*Ferroelectrics*, 464:42–48, 2014

ISSN: 0015-0193 print / 1563-5112 online
DOI: 10.1080/00150193.2014.892811

Taylor & Francis
Taylor & Francis Group

# Study of Physical Properties of $Ba(Ti_{1-2x}Fe_xNb_x)O_3$ Ceramics

C. KAJTOCH,[1,*] W. BAK,[1] B. GARBARZ-GLOS,[1]
K. RUEBENBAUER,[1] A. BLACHOWSKI,[1] D. ZIETEK,[1]
T. CZEPPE,[2] AND K. MROCZKA[3]

[1]Institute of Physics, Pedagogical University, Cracow, Poland
[2]Institute of Metallurgy and Materials Science, Polish Academy of Sciences, Cracow, Poland
[3]Institute of Technical Science, Pedagogical University, Cracow, Poland

*$Ba(Ti_{1-2x}Fe_xNb_x)O_3$ (abbreviated to BTFNx) solid solutions were prepared by a conventional solid state reaction method. The results of the structural, microstructural, dielectric and Mossbauer investigations of the polycrystalline samples with* $x = 0, 0.05, 0.10$ *and* $0.33$ *are presented. The EDS studies revealed that the samples were well sintered and that the material was chemically homogeneous. The transformation from the normal to the relaxor ferroelectric state with the increase of Fe and Nb ions content was observed.*

**Keywords** ceramics; ferroelectric properties; phase transitions; Mössbauer effect

## Introduction

Barium titanate (BT) with perovskite structure is still interesting for many researchers because of the fact that it possesses a high dielectric permittivity at room temperature, large piezoelectric and pyroelectric coefficients, comparable with lead based perovskite ferroelectrics, does not contain toxic elements and it is characterized by relatively low production costs. Not without significance is the fact that its electrical properties can be controlled within a wide range by means of various elemental additions, what results in enhanced control over dielectric characteristics. These characteristics depend on the type of the substitution, isovalent or heterovalent ions and its location in the crystal sub-lattice: for Ba (A-site) or for Ti (B-site). It is known from the literature [1–10], that in case of the B-site substitution, substantial replacement of $Ti^{4+}$ by any of the three ions $Zr^{4+}$, $Sn^{4+}$ or $Hf^{4+}$ affects the transition temperatures. In case of the content of zirconium, tin or hafnium higher than 15 %, all observed temperatures of the transitions from rhombohedral to orthorhombic, orthorhombic to tetragonal and tetragonal to cubic structures move closer with increase of the content of such elements and finally merge into one. In the early studies it was reported [11–18], that additions of transition metals like Nb, Fe or Mn also influence

Received September 2, 2013; in final form November 6, 2013.
*Corresponding author. E-mail: ckajtoch@up.krakow.pl
Color versions of one or more of the figures in the article can be found online at www.tandfonline.com/gfer.

phase formation, microstructure and electrical properties of the BT ceramics. Hence, in the present study, the simultaneous influence of Nb and Fe additions on the physical properties of BT including phase transitions was investigated and discussed.

## Experimental

$BaC_2O_4$, $TiO_2$, $Fe_2O_3$ and $Nb_2O_5$ powders were mixed, dried and pressed by 0.3 GPa unaxial pressure. The polycrystalline BTFNx sample, 8 mm in diameter, 1.5 mm in thickness, was synthesized at 1250 K and sintered, after re-milling at 1510 K. The Hitachi S4700 scanning electron microscope (SEM) coupled with EDS (Energy-Dispersive X-Ray Spectroscopy) was used to investigate microstructure and chemical composition of the samples. EPMA (Electron Probe Micro - Analyser) was applied to the analysis of the distribution of elements on the samples surfaces. The method of Mössbauer spectroscopy was applied. The MsAa-3 spectrometer was used with the Kr-filled proportional counter and commercial $^{57}$Co (Rh) source. Velocity scale was calibrated by the Michelson-Morley interferometer equipped with the He-Ne laser. The line of $^{57}$Fe, 14.4-keV was used. The spectra were collected at room temperature in the transmission mode, calibrated and processed by means of the Mosgraf-2009 suite proper applications. In the paper all spectral shifts are reported in relation to $\alpha$-Fe lines, room temperature positions. For dielectric measurements the samples were covered with the silver electrodes. The dielectric measurements were performed with use of Alpha-AN High Performance Frequency Analyzer system equipped with cryogenic temperature control by Quatro Cryosystem and WinDETA Novocontrol software. The measurements were made during cooling at the rate of 2 K/min, in the frequency range from 0.1 Hz to 10 MHz.

## Results and Discussion

The SEM micrographs of the BTFNx ceramics with $x = 0.05$ and 0.10 are shown in Fig. 1. The SEM image for the composition of $x = 0.05$ (Fig. 1a) shows a non-uniform microstructure with bimodal grain size distribution. Larger grains coexist with the smaller and with a certain amount of intergranular pores. For BTFNx ceramics with $x = 0.10$ (Fig. 1b) the bimodal microstructure consisting of well grown plate-like grains embedded in an equiaxial grained matrix was revealed. In Fig. 2 the EDS spectra from the chosen microregions of the BTFNx sample with $x = 0.10$ are shown. In the spectra nothing more than the expected elements can be seen. Fig. 3 presents the distribution of elements on the

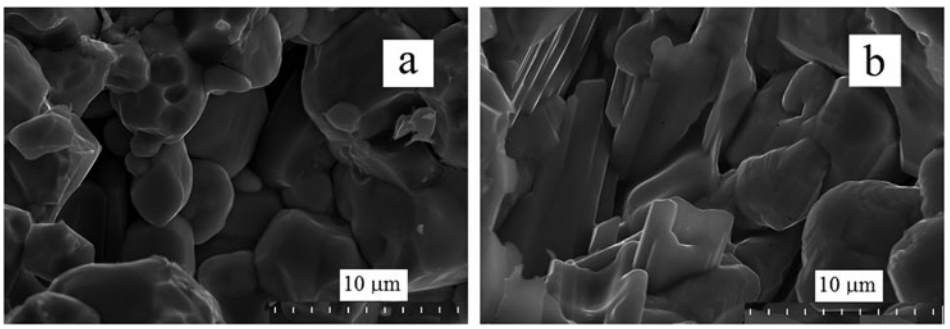


**Figure 1.** SEM micrograph of BTFN5 (a) and BTFN10 (b) (magn. 5000×).

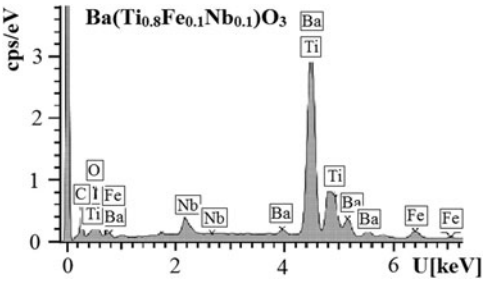


**Figure 2.** Elemental composition from EDS measurements for BTFN10.



polished surface of the same sample performed with use of EPMA in the mapping mode. This investigations exhibited homogenous distribution of the ions of O, Ti, Fe, Nb and Ba in the polycrystalline material. The next figure shows the temperature dependence of the real part of the electric permittivity $\varepsilon$' (Fig. 4(a)) and inverse electric permittivity $\varepsilon'^{-1}$ (Fig. 4(b)) for pure BT and BTFNx samples. The increase in the concentration of Fe and Nb to the value of $x = 0.05$ causes increase of the phase transition temperature and a small decrease in the maximum value of the real part of the electric permittivity. For this composition two phase transitions were observed. A little diffuse about 450 K and strongly diffused below 200 K. For the value of $x = 0.10$ a significant reduction both of the maximum values of the electric permittivity and the corresponding temperature was noted. The analysis of the experimental data shows that all three phase transitions corresponding to the pure BT were unified into single phase transition in the BTFNx with $x = 0.10$ sample. Moreover, for this sample a diffuse phase transition of a relaxation type (inset in Fig. 4(a)) was observed. This suggests that the additions of the $Fe^{3+}$ and $Nb^{4+}$ ions in the sub-lattice B, to the BT gives stable electrical system and allows to increase the concentration of Fe up to $x = 0.10$, with maintaining the ferroelectric properties. The sample BTFNx with

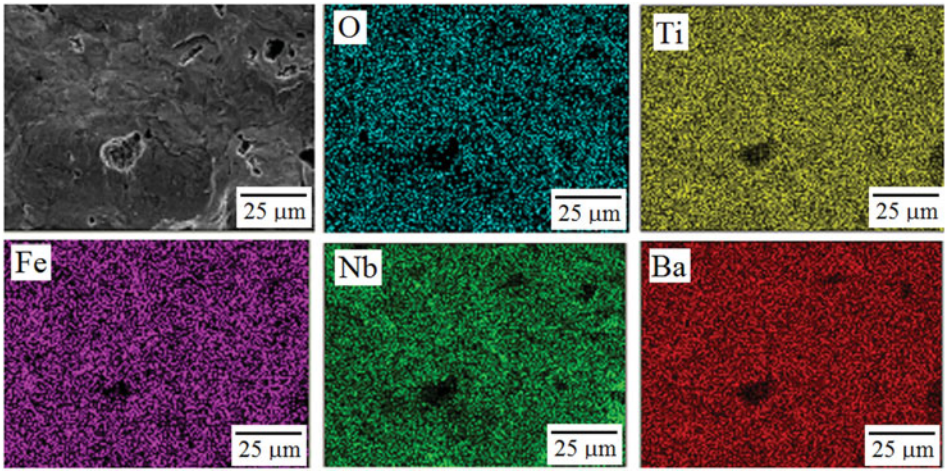


**Figure 3.** The photograph of a surface fragment of BTFN10 sample (a) on which the mapping using EPMA was performed (enlargement by1000×) and distribution of (b) oxygen O, (c) titanium Ti, (d) iron Fe, (e) niobium Nb and (f) barium Ba on the sample surface.

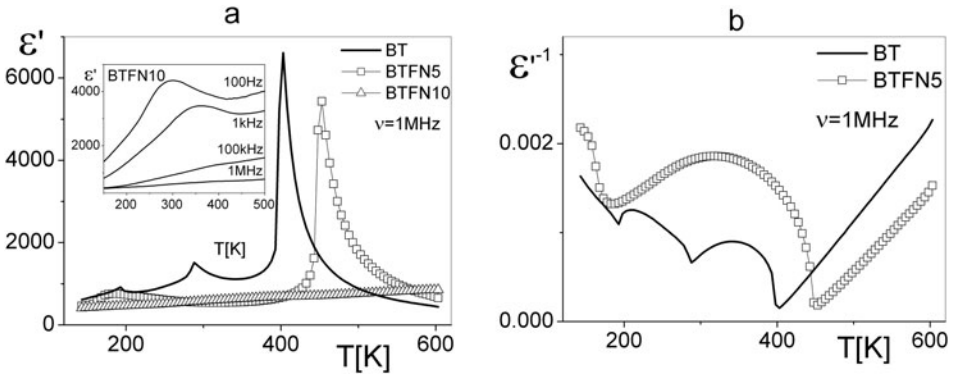


**Figure 4.** Temperature dependence of $\varepsilon'$ (a) and $\varepsilon'^{-1}$ (b) for BT and BTFNx, $\nu = 1$MHz.

$x = 0.33$, in the investigated range of temperatures does not exhibit ferroelectric behavior. In paraelectric phase, for BTFNx samples with $x = 0$ and 0.05, linear dependence of the inverse of electric permittivity versus temperature was observed. X-ray measurements (Fig. 5) confirmed that Fe and Nb ions lead to the freezing of the high temperature cubic paraelectric phase. Fig. 5 shows the results of XRD measurements in case of the BTFNx, with $x = 0.33$, confirming the existence of the regular crystallographic structure at room temperature. The absence of the paraelectric–ferroelectric (PE–FE) phase transition in dielectric measurements also confirms this result. In the BTFNx ceramics the distribution of Nb and Fe ions in B-site is rather random, what was confirmed by measurements of the Mössbauer effect, and the trivalent iron ion is more stable than the niobium ion, thus this situation favors generation of the oxygen vacancies. For small concentrations of iron, trapped electrons are mainly derived from donor centers. Increasing the iron content leads to an increase in the number of trapped electrons from the valence band and thus increases the value of the dielectric loss. Random distribution of Nb and Fe ions in B-site also has a very strong influence on the nature of the PE–FE phase transition, as a result for higher concentrations of both ions diffuse phase transitions were observed. Relevant Mössbauer spectra are shown in Fig. 6, while essential Mössbauer parameters are listed in Table 1. The absorption cross-section could be described by the contributions from the symmetric

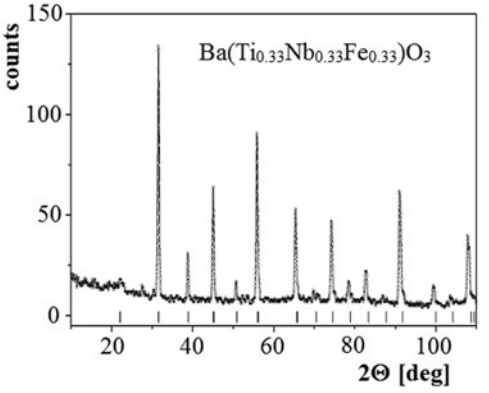


**Figure 5.** X-ray diffraction pattern for BTFNx, with $x = 0.33$ at room temperature.

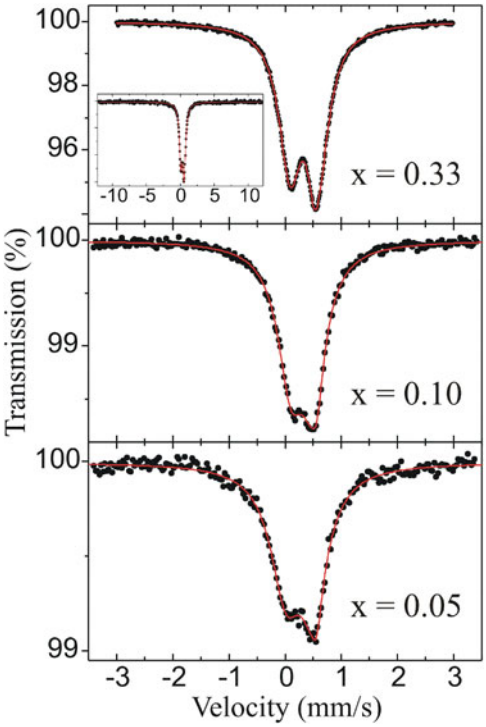


**Figure 6.** Mössbauer spectra of the samples with $x = 0.33$, 0.10 and 0.05. Inset shows spectrum obtained in the larger scale of velocity for the sample with $x = 0.33$.

electric quadrupole doublet and a singlet, the last one being the minor component – about 5%. Iron ions remain in the high-spin trivalent state in both sites. The relative proportions of occupied positions in both sites are independent on the actual iron content in the sample. Hence, one can conclude that the minority phase exhibiting singlet is some iron-niobium oxide with the highly trivalent iron (revealing high isomer shift) residing in the perfect cubic environment (singlet with narrow line). The hyperfine parameters of this site remain practically constant for all samples. A total shift of the doublet increases systematically with the lowering of the iron content. This means that the isomer shift increases with the iron dilution leading to the more extreme trivalent state i.e. the electron density on the iron

**Table 1**
Essential parameters of the Mössbauer spectra obtained at room temperature

| $x$ | A [%] | S [mm/s] | $\Delta$ [mm/s] | $\Gamma$ [mm/s] |
|---|---|---|---|---|
| 0.33 | 95 | 0.45 | 0.49 | 0.37 |
| | 5 | 0.63 | | 0.12 |
| 0.10 | 95 | 0.41 | 0.38 | 0.47 |
| | 5 | 0.69 | | 0.12 |
| 0.05 | 95 | 0.37 | 0.47 | 0.56 |
| | 5 | 0.68 | | 0.12 |

nucleus decreases with the increasing dilution. An electric field gradient tensor (EFG) is present on the iron nucleus for all iron concentrations. Hence, it seems that the oxygen octahedron around the iron ion is distorted from the cubic symmetry regardless of the iron concentration. This distortion exhibits some local character due to the presence of the foreign iron atom instead of the expected tetravalent titanium atom. It should be noted that EFG for the high-spin trivalent iron is generated primarily by the lattice distortion. The charge compensation occurs on somewhat larger scale due to the presence of pentavalent niobium ions substituting titanium. Absorber line width is large and increases significantly with the iron dilution. Hence, one can conclude that iron resides close to the lattice defects generating distribution of EFG. For high iron content defect sites are not available for all iron atoms and some narrowing of the absorber line width is observed. These defects act as acceptors diminishing electron density on the iron nucleus by 0.02 el./(a.u.)$^3$ [19], while going from the sample with $x = 0.33$ to the sample with $x = 0.05$. No magnetically ordered phases containing iron were found at room temperature for any sample (see inset in Fig. 6). Essential parameters of the Mössbauer spectra obtained at room temperature for the samples with $x = 0.33$, 0.10 and 0.05 are given in Table 1. The parameter A denotes relative contribution of the two iron sites to the absorption cross-section. The parameter S stands for the total spectral shift versus $\alpha$-Fe standard, at room temperature, while the parameter $\Delta$ denotes the electric quadrupole splitting. Finally, the parameter $\Gamma$ stands for the absorber line width.

## Conclusions

The EDS and EPMA investigations confirmed the high purity of the samples and the expected quantitative compositions. Dielectric measurements showed that the addition of niobium and iron ions in the sub-lattice B in the $ABO_3$ crystal lattice of barium titanate changed the nature of the phase transitions. For BT and BTFNx sample with $x = 0.05$, the sharp PE–FE phase transitions were observed, whereas for BTFNx sample with $x = 0.10$ the relaxor type phase transition occurred. The results of Mössbauer effect obtained allow to assume that the material with the stable electrical and magnetic properties may be obtained.

## References

1. A. Bootchanont, J. Jutimoosik, S. Chandarak, M. Unruan, S. Rujirawat, R. Yimnirun, R. Guo, and A. Bhalla, Investigation of local structure in $BaTiO_3$-$BaZrO_3$ system by synchrotron X-ray absorption spectroscopy. *Ceram Int*. **39**, S579–S582 (2013).
2. C. Kajtoch, Influence of Zr-substitution on phase transitions character in polycrystalline $Ba(Ti_{1-x}Zr_x)O_3$. *J Mater Sci*. **46**, 1469–1473 (2011).
3. F. Moura, A. Z. Simoes, B. D. Stojanovic, M. A. Zaghete, E. Longo, and J. A. Varela, Dielectric and ferroelectric characteristics of barium zirconate titanate ceramics prepared from mixed oxide method. *J Alloy Compd*. **462**, 129–134 (2008).
4. B. Garbarz-Glos, K. Bormanis, and D. Sitko, Effect of $Zr^{4+}$ doping on the electrical properties of $BaTiO_3$ ceramics. *Ferroelectrics*. **417**, 118–123 (2011).
5. C. Kajtoch, Dielectric properties of $Ba(Ti_{1-x}Sn_x)O_3$ ceramics in the paraelectric phase. *Ceram Int*. **37**, 387–391 (2011).
6. V. V. Shvartsman, J. Dec, Z. K. Xu, J. Banys, P. Keburis, and W. Klemann, Crossover from ferroelectric to relaxor behavior in $BaTi_{1-x}Sn_xO_3$ solid solution. *Phase Trans*. **81**, 1013–1021 (2008).
7. C. Kajtoch, Dipolar polarization in $Ba(Ti_{1-x}Sn_x)O_3$. *Ferroelectrics*. **172**, 465–468 (1995).

8. W. Bąk, C. Kajtoch, and F. Starzyk, Dielectric properties of $Ba(Ti_{1-x}Sn_x)O_3$ solid solution, *Mat Sci Eng B*. **100**, 9–12 (2003).
9. B. Garbarz-Glos, W. Piekarczyk, I. Smeltere, W. Śmiga, and M. Antonova, Ultrasonication as a Method of Investigation of the Mechanical Properties of Doped Hafnium Barium Titanate. *Ferroelectrics*. **436**, 87–95 (2012).
10. S. Anwar, P. R. Sagdeo, and N. P. Lalla, Ferroelectric relaxor behavior in hafnium doped barium-titanate ceramic. *Sol. St. Comm*. **138**, 331–336 (2006).
11. E. Brzozowski, M. S. Castro, Grain growth control in Nb-doped $BaTiO_3$. *J Mater Proc Tech*. **168**, 464–470 (2005).
12. N. Maso, H. Beltran, E. Cordoncillo, D. C. Sinclair, and A. R. West, Polymorphism and dielectric properties of Nb-doped $BaTiO_3$. *J Am Ceram Soc*. **91**, 44–150 (2008).
13. N. Maso, H. Beltran, E. Cordoncillo, A. A. Flores, P. Escribano, D. C. Sinclair, and A. R. West, Synthesis and electrical properties of Nb-doped $BaTiO_3$. *J Mater Chem*. **16**, 3114–3119 (2006).
14. A. Jana, T. K. Kundu, S. K. Pradhan, D. Chakravorty, Dielectric behavior of Fe-ion-doped $BaTiO_3$ nanoparticles. *J Appl Phys*. **97**, 044311–1-6 (2005).
15. N. Maso, H. Beltran, E. Cordoncillo, P. Escribano, and A. R. West, Electrical properties of Fe-doped $BaTiO_3$. *J Mater Chem*. **16**, 1626–1633 (2006).
16. S. H. Yoon, C. A. Randall, and K. H. Hur, Difference between resistance degradation of fixed valence acceptor (Mg) and variable valence acceptor (Mn)-doped $BaTiO_3$ ceramics. *J Appl Phys*. **108**, 064101–1-9 (2010).
17. H. Gong, X. Wang, S. Zhang, Z. Tian, and L. Li, Electrical and reliability characteristics of Mn-doped nano $BaTiO_3$-based ceramics for ultrathin multilayer ceramic capacitor application. *J Appl Phys*. **112**, 114119–1-6 (2012).
18. D. Sitko, W. Bąk, B. Garbarz-Glos, M. Antonova, and I. Jankowska-Sumara, Effect of $MnO_2$ doping on the dielectric properties of barium titanate ceramics. *Ukr J Phys Opt*. **13**, 34–43 (2012).
19. U. D. Wdowik, K. Ruebenbauer, Calibration of the isomer shift for the 14.4-keV transition in $^{57}Fe$ using the full-potential linearized augmented plane-wave method. *Phys Rev B*. **76**, 155118–1-6 (2007).